JPhys Materials

PURPOSE-LED PUBLISHING™

PAPER • OPEN ACCESS

In situ engineering hexagonal boron nitride in van der Waals heterostructures with selective SF_6 etching

To cite this article: Hitesh Agarwal *et al* 2025 *J. Phys. Mater.* **8** 045006

Journal of Physics: Materials

OPEN ACCESS

RECEIVED
9 December 2024

REVISED
18 July 2025

ACCEPTED FOR PUBLICATION
19 August 2025

PUBLISHED
10 September 2025

PAPER

In situ engineering hexagonal boron nitride in van der Waals heterostructures with selective SF_6 etching

Hitesh Agarwal[1], Antoine Reserbat-Plantey[1,2,*], David Barcons Ruiz[1], Karuppasamy Pandian Soundarapandian[1], Geng Li[1], Vahagn Mkhitaryan[1], Johann Osmond[1], Helena Lozano[1], Kenji Watanabe[3], Takashi Taniguchi[4], Petr Stepanov[1,5], Frank H L Koppens[1,6,*] and Roshan Krishna Kumar[1,7,*]

[1] ICFO—Institut de Ciències Fotòniques, The Barcelona Institute of Science and Technology, Av. Carl Friedrich Gauss 3, Castelldefels (Barcelona), 08860, Spain
[2] Université Côte d'Azur, CNRS, CRHEA, rue Bernard Grégory, 06560 Valbonne, France
[3] Research Center for Functional Materials, National Institute for Materials Science, Tsukuba 305-0044, Japan
[4] International Center for Materials Nanoarchitectonics, National Institute for Materials Science, Tsukuba 305-0044, Japan
[5] Department of Physics and Astronomy, University of Notre Dame, Notre Dame, IN 46556, United States of America
[6] ICREA—Institució Catalana de Recerca i Estudis Avancats, 08010 Barcelona, Spain
[7] Catalan Institute of Nanoscience and Nanotechnology (ICN2), Campus UAB, Bellaterra, 08193 Barcelona, Spain
[*] Authors to whom any correspondence should be addressed.

E-mail: antoine.reserbat-plantey@cnrs.fr, frank.koppens@icfo.eu and roshan.krishna@icn2.cat

Keywords: 2D Materials, graphene, nanofabrication, van der Waals heterostructures, nanopatterning

Supplementary material for this article is available online

Abstract

Van der Waals heterostructures are at the forefront in materials heterostructure engineering, offering the ultimate control in layer selectivity and capability to combine virtually any material. Hexagonal-boron nitride, the most commonly used dielectric material, has proven indispensable in this field, allowing the encapsulation of active 2D materials preserving their exceptional electronic quality. However, not all device applications require full encapsulation but rather require open surfaces, or even selective patterning of hBN layers. Here, we report on a procedure to engineer top hBN layers within van der Waals heterostructures while preserving the underlying active 2D layers. Using a soft selective SF_6 etching combined with a series of pre—and post-etching treatments, we demonstrate that pristine surfaces can be exposed with atomic scale flatness while preserving the active layers' electronic quality. We benchmark our technique using graphene/hBN Hall bar devices. Using Raman spectroscopy combined with quantum transport, we show high quality can be preserved in etched regions by demonstrating low temperature carrier mobilities $> 200{,}000\ \mathrm{cm^2V^{-1}s^{-1}}$, ballistic transport probed through magnetic focusing, and intrinsic room temperature phonon-limited mobilities. Atomic force microscopy brooming and O_2 plasma cleaning are identified as key pre-etching steps for obtaining pristine open surfaces while preserving electronic quality. The technique provides a clean method for opening windows into mesoscopic van der Waals devices that can be used for local probe experiments, patterning top hBN *in-situ*, and exposing 2D layers to their environment for sensing applications.

The synthesis of high-quality hexagonal-boron nitride [1] marked a turning point in two-dimensional (2D) materials research [2–4]. As an inert 2D crystal, it is an excellent dielectric material in 2D electronics [5], provides atomically flat surfaces with pristine interfaces [6], and protects active 2D layers from degrading atmospheric environments [7]. These properties enable engineering van der Waals heterostructures of the highest quality with unique functionalities envisioned for next-generation semiconductor technologies [8]. Additionally, they serve as powerful condensed matter simulators harboring physics spanning strongly correlated electron phenomena to topological physics [9]. In most van der Waals heterostructures, hBN typically encapsulates active 2D layers. The bottom hBN protects layers from rough substrates [10], while the top isolates it completely from its environment, pushing device quality to intrinsic limits [11]. However,

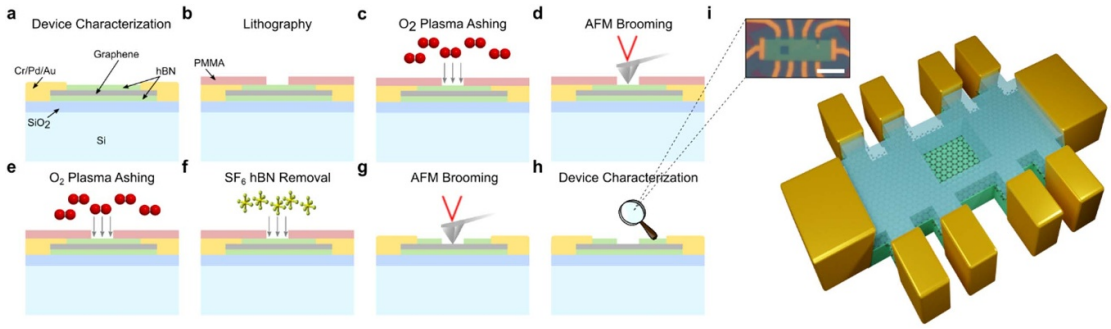

Figure 1. Methods for *in-situ* engineering top hexagonal-boron nitride in van der Waals heterostructures. (a)–(h), schematics of the work flow presented in this work. The device schematic is sketched in a, showing a graphene (grey) encapsulated with hBN (green), contacted with Chromium, palladium, gold (Cr/Pd/Au) and fabricated on a silicon dioxide (SiO_2) on silicon (Si) substrate which was used as an electrostatic gate. A series of lithography (b), O_2 plasma ashing (c), (e) and dry etching (f) is performed. At specific steps, AFM brooming is employed (d), (g) to remove contaminants and preserve electronic quality. (i) optical image of our device D1 after a window has been opened. Scale bar is 10 μm.

certain applications and experiments require exposed surfaces. Hence, full encapsulation is not always desirable because it restricts access to active 2D layers.

From an applications perspective, exposed surfaces offer advantages and novel functionalities, such as tailoring light-matter interactions via patterned metasurfaces [12], leveraging 2D materials' surface sensitivity for biological and chemical sensing [13] and ensuring good electrical and magnetic contacts [14]. From a fundamental standpoint, exposed surfaces allow direct access to the underlying electron system using local probes. Some of the most powerful local spectroscopic probes, including scanning tunneling microscopy [15–18] and Angle-resolved photoemission spectroscopy [19, 20], require exposed 2D layers achievable only through challenging heterostructure engineering. These techniques limit scanning areas and suffer from polymer contamination which may degrade sample quality. In all these applications and experiments, the bottom hBN remains crucial playing a major role in preserving electronic quality.

To overcome these challenges, we introduce an *in-situ* hBN patterning method for van der Waals heterostructures. We demonstrate that sulfur hexafluoride (SF_6) can selectively etch [21] the top hBN in encapsulated heterostructures, opening windows into small regions of the device (figure 1) that serve as access points to the underlying 2D layers. Using graphene encapsulated with hexagonal-boron nitride, we track the quality of selectively etched regions through atomic force microscopy (AFM), Raman spectroscopy and quantum transport measurements, demonstrating that high electronic quality remains intact, limited by atmospheric conditions. The methodology is sketched in figures 1(a)–(h). Starting with fully encapsulated hBN/graphene/hBN devices with electrical contacts (figure 1(a)), we pattern etching masks (figure 1(b)) with PMMA. Following, a series of cleaning steps including O_2 plasma etching and AFM brooming (figures 1(c)–(e) prepares the surface for SF_6 etching of hBN (figure 1(f)).

SF_6 has proven highly effective in graphene nanofabrication due to its ability to selectively etch hBN without damaging graphene, enabling controlled exposure of clean graphene edges [22]. When used as an etchant for hBN, the energetic plasma breaks SF_6 molecules, generating reactive fluorine radicals. These fluorine atoms react with the boron in the BN lattice forming volatile boron trifluoride (BF_3), while the nitrogen is released as molecular nitrogen [21] (N). In a simplified overall reaction, one may write: $2\mathrm{BN}\,(\mathrm{s}) + 6F \rightarrow 2BF_3\ (g) + N_2\,(g)$ where (s) and (g) refer to solid and gas phase respectively. In the plasma process, fluorine atoms come from SF_6, which is reduced to SF_4 or other sulfur-fluoride species. The main etch products are boron trifluoride (BF_3), removed as a volatile gas, and nitrogen (N_2) released into the atmosphere. Because of its excellent selectivity for hBN over graphene, it is commonly used to create low-resistance electrical contacts [22]. Here, we use it instead to directly pattern the top encapsulating hBN layers, selectively removing specific areas that expose the underlying graphene (figure 1) while preserving the bottom hBN substrate and maintaining graphene's high electronic quality.

In this work, we use a recipe inspired by previous works [21, 22]. However, we introduce additional pre-etching steps and refine the etching procedure to optimize graphene's electronic quality (see supplementary section 1), making it suitable for various applications and experiments. While SF_6 etching stops at graphene, over-etching may still be detrimental, leading to fluorination or doping inhomogeneities. Calibrating etching time and recipes across different reactive ion etchers (RIE) is crucial to ensure selective hBN removal without excessive graphene fluorination. Generally, a stable plasma should be maintained with the highest chamber pressures but lowest radio frequency powers. Higher pressures reduce precision but enable slower, more controlled hBN removal, essential for preserving graphene's electronic quality. We

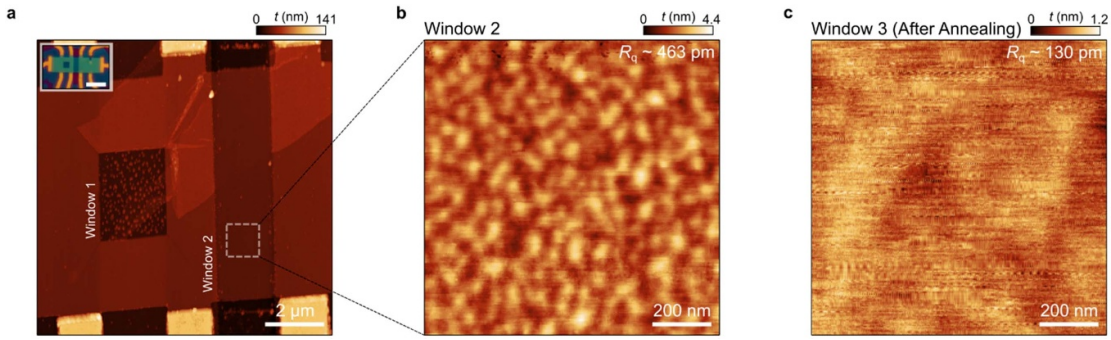

Figure 2. Atomic force microscopy measurements of etched regions. (a) an AFM image of device 1 in the regions where D1_window1 and D1_window2 have been opened (see white labels). The gold regions with the largest height (t) correspond to the electrical contacts of the device. The inset displays an optical image of the device. The scale bar is 2 μm. (b) Zoomed spatial map of the height profile (t) in D1_window 2. The area is indicated by the white dashed box in panel **a**, (c), a 1 × 1 μm^2 area of D2_window3 after annealing.

perform systematic calibration using reference regions on hBN layers and use optical microscopy to track the hBN removal during sequential etching steps until complete. The calibrated recipe can then be applied to the active region. We characterize our devices in the etched regions before and after exposure of graphene to benchmark its electronic quality and the importance of the steps employed in b–g.

To develop the selective etching recipe, we studied graphene-based/hBN heterostructures. This included two monolayer graphene devices encapsulated with hBN (D1/2) and a small angle twisted bilayer graphene device (D3). All devices were fabricated using standard methods (see methods). The process involved heterostructure assembly, followed by nanofabrication of mesoscopic devices with Hall bar geometries (figure 1(i)). Low-temperature (10 K) quantum transport measurements characterized the devices, revealing excellent electronic quality, including size-limited mobilities [23, 24] (see discussions below). All devices were studied before and after etching using AFM. However, Raman spectroscopy and quantum transport measurements post-etching were performed exclusively on monolayer graphene/hBN heterostructures because of its well-known electronic properties which enabled proper calibration.

Following low-temperature device characterization, we applied our selective etching method. Optimized recipes, discussed in methods and supplementary section 1, were tested on all devices. Here, we present results on hBN/Graphene/hBN devices, where three windows were opened on two devices-D1 (figure 2(a)) and D2 (figure 2(c))-demonstrating the importance of pre- and post-etching steps. The first is a small square on the device's left side (figure 2(a)). For this window (D1_window1), we follow steps figures 1(b)–(f), directly etching the device after patterning the PMMA mask. The second window (D1_window2) extends the entire device width. In this case, additional pre-etching steps were used, where the top hBN surface was first cleaned using AFM brooming [25–27] to remove polymer residues from the targeted region (figures 1(d) and (e)), followed by O_2 plasma cleaning. The third window in D2 (D2_window3) followed the same procedure, but was additionally annealed under ultra-high vacuum post-etching.

All three windows were characterized using AFM. Figure 2(a) plots a topographic map of D1 after etching windows 1 and 2. The two regions exhibit notable differences. D1_window1 shows significant surface roughness resembling contaminants accumulating on the surface of graphene. In contrast, the D1_window2 appears much smoother with a root square mean roughness (R_q) below 1 nm. Figure 2(b) further illustrates this by plotting the height profile (t) as a function of x,y spatial coordinates for a 1 × 1 μm^2 areas. We attribute these differences to the crucial importance of AFM brooming. Without brooming, any surface contamination on the top hBN falls onto the graphene. With brooming the top hBN can be cleaned enabling selective etching that exposes the graphene with a pristine surface. The residual surface roughness tells us that some contamination still remained, possibly due to hydrocarbon adsorbates or PMMA residues. Following the same procedure in a third device (D3_window4), we achieved atomically flat areas ($R_q = 0.2$ nm) over 1 × 1 μm^2 areas (see supplementary section 2). With additional post-etching annealing in D2_window3, even smoother surfaces were achieved. This included atomically flat areas over 2 × 2 μm^2, meeting the requirements of sensitive scanning probe experiments (figure 2(c)).

While AFM measurements suggest clean exposed surfaces can be achieved, the chemical procedure may fluorinate graphene or degrade its crystalline quality, which AFM alone cannot easily detect. Therefore, we performed micro-Raman spectroscopy to characterize the exposed graphene's quality further, compare it with the fully encapsulated graphene, and evaluate the impact of etching. We focus on the E_{2g} Raman active modes, leading to the G band [28] at around 1582 cm^{-1}, and for hBN [29] at 1362 cm^{-1}. Notably, we

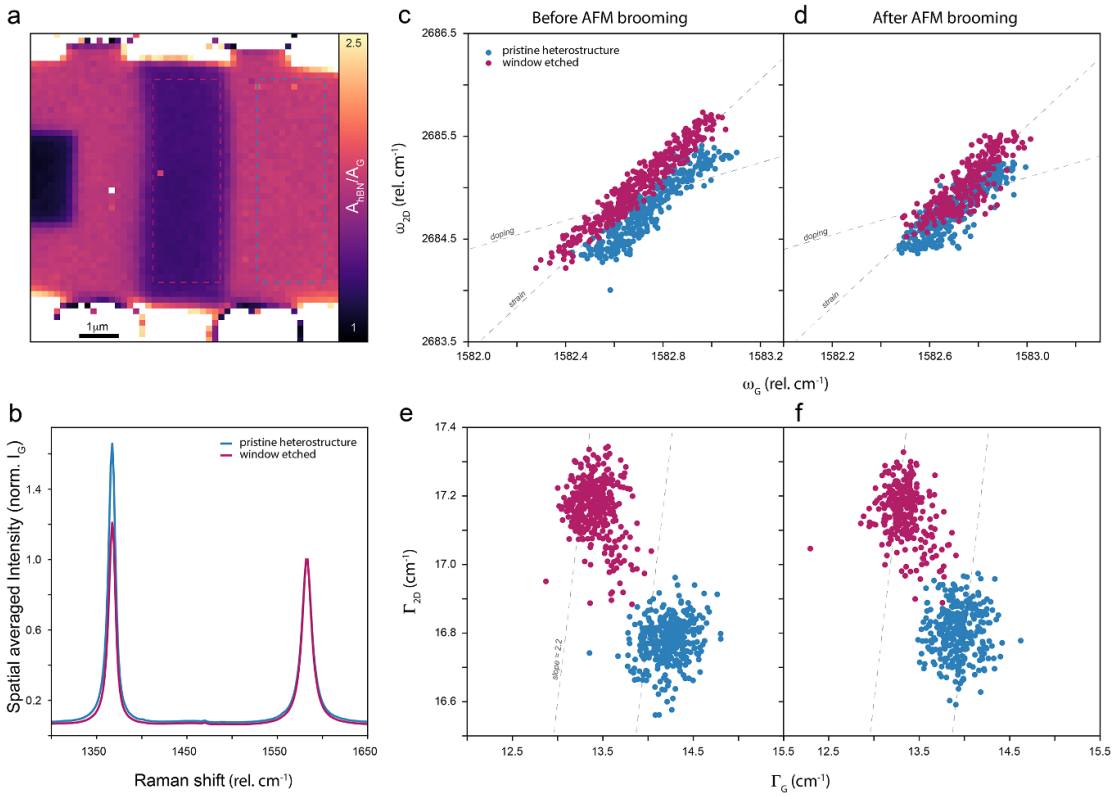

Figure 3. Investigation of window opening and surface brooming effects on graphene via micro-Raman spectroscopy (a): Hyperspectral Raman map of the sample displaying the amplitude of the hBN E_{2g} peak normalized by the amplitude of the graphene *G* peak, which mitigates interference effects. The zones highlighted in pink including the left square area, correspond to regions where the top hBN layer has been removed (etched windows) (b): Spatially averaged Raman spectra of the E_{2g} modes for hBN and the graphene *G* band. The spatial averages correspond to the pink (etched windows, D1_window2) and blue (fully encapsulated heterostructure) regions indicated in panel **a** (c) and (d): Correlation plots of the positions of the graphene G and 2D bands before (c) and after (d) AFM brooming. The pink and blue data points correspond to the etched windows and fully encapsulated areas shown in panel **a**, respectively. The black dashed lines represent theoretical predictions of (ω_G, ω_{2D}) for graphene under constant doping and uniform strain [35] (e) and (f): Similar correlation plots as in panels **c** and **d**, but showing the relationships between the linewidths of the G and 2D peaks. The dashed lines, with a slope of 2.2, correspond to the expected trend for strain-induced broadening of the Raman peaks [10], illustrating the increased broadening due to strain variations within the laser spot area.

observed the 2D band in our exfoliated graphene monolayer sample, with intensity more than 5*x* times larger than the *G* band and with a Lorentzian profile, an indicator of weakly doped monolayer graphene [30] (supplementary information 3). At no point did we detect the emergence of the D or D' bands from graphene [31], even after opening the hBN window (figure 3(b)). This absence of the defect bands suggests good preservation of the crystalline structure after etching and therefore negligible fluorination.

We first performed hyperspectral mapping of the sample (figure 3(a)), wherein the laser spot (500 nm diameter) was scanned over the device, and a spectrum was recorded at each point. We identified the etched zones—D1_window1/2—by plotting the hBN E_{2g} phonon peak area (A_{hBN}) centred at 1362 cm^{-1} (figure 3(b)) defined as $A_{hBN} = \pi/2\ (I_{hBN}\Gamma_{hBN})$, where I_{hBN} and Γ_{hBN} refer to the peak intensity and peak width respectively. Removing hBN material alters the optical planar cavity formed by the heterostructures on the SiO_2 dielectric and the back silicon mirror [32]. The interferences, governed by the local optical gain dependent on different layers' thicknesses and refractive indices, affect the pump laser (at 532 nm) and the Raman scattered light [33]. Consequently, the net interference pattern can be complex [34]. To better observe the effect of removing the hBN top layer, we normalized the hBN peak area by the G band area, assuming it remains constant during etching. This assumption is supported by the absence of the D band post etching, suggesting good preservation of sp^2 carbon bonds and confirming graphene's crystalline integrity [34]. We report a $\sim$ 35% reduction in the hBN area signal in the window zone (figure 3(b)). Interestingly, a 55% decrease was expected, given the top hBN thickness of 17.5 nm and the bottom of 14 nm (measured via AFM). This discrepancy may result from normalizing by the *G* band area, which does not fully eliminate the Raman interference effect, as there is still a small shift in the scattered light wavelength between the two peaks.

To further analyse the quality of graphene after the etching, we plotted the correlation between the *G* and 2D band positions [35] (figure 3(c)), isolating clusters of points corresponding to the D1_window2 area

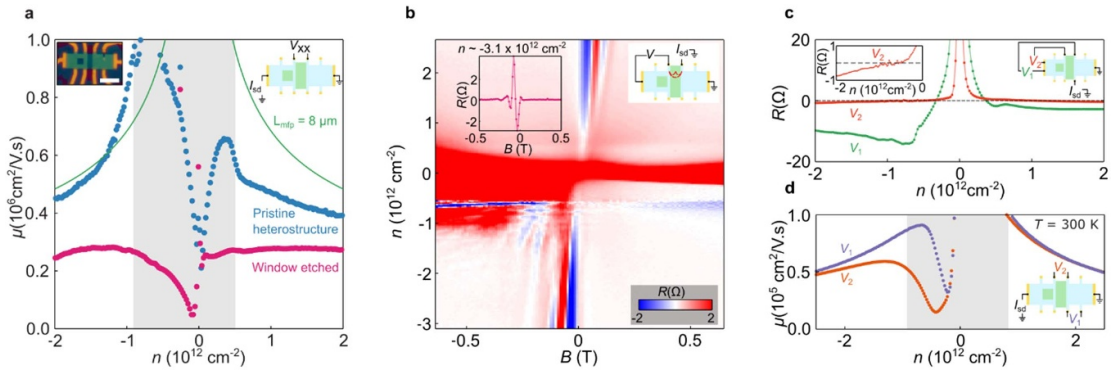

Figure 4. Quantum transport measurements in etched region (a), mobility (μ) as a function of carrier doping (n) measured at 10 K in the same region of the device before (blue circles) and after (pink circles) etching D1_window1 and D2_window2. The green solid line traces the device width limited mobility. The top right inset sketches the measurement geometry. (b), Magnetic focusing resistance R_{TMF} plotted as a function of carrier doping (n) and magnetic field (B) at 10 K. Top left inset plots a line cut for carrier density $n = -3.1 \times 10^{12}$ cm^{-2}. Top right inset sketches the measurement geometry. (c) Bend resistance R_B plotted as a function of carrier doping n at 10 K for two geometries V_1 and V_2. Top right inset sketches the measurement geometries. (d), $\mu(n)$ measured around D1_window2 (orange) and in the fully encapsulated region (purple) at 300 K.

(pink) and the fully encapsulated zone (blue). The two rectangular zones are shown in figure 3(a). Although both clusters are close, we observe a systematic shift typically linked to doping differences between regions. This shift aligns with a local change in the Fermi level due to contaminant absorption directly on graphene or fluorination [35]. Following the framework analysis of previous works [10, 35], which shows doping around 0.1×10^{12} cm^{-2}, consistent with our low-temperature quantum transport measurements (see supplementary section 5). In contrast, encapsulated graphene remains protected from the environment. In both cases, data clusters elongate along the strain axis, indicating the strain distribution is not perfectly uniform across the scanned area [10]. Interestingly, elongation is more pronounced in the etched window, suggesting that removing the top encapsulant caused a local strain redistribution within the monolayer.

We then performed an additional step called AFM brooming, where an AFM tip in scanning contact mode cleans the exposed surface, acting as a nanoscale broom. We repeated the same Raman analysis after brooming (figure 3(d)) and observed that the data clusters almost perfectly overlap, indicating efficient removal of contaminants and a nearly identical Fermi level in both etched and encapsulated areas. Further Raman correlation analysis, comparing G and 2D linewidths (figures 3(e) and (f)), provides insight into strain distribution at the nanoscale [10]. Here, we observe a clear difference in strain distribution between the fully encapsulated pristine heterostructure and the etched window. The higher center position of the data cluster for the etched window suggests more inhomogeneous strain distribution at the nanoscale, varying over a smaller length scale than in the fully encapsulated case. At first glance, this may seem unexpected since encapsulation between hBN layers initially established graphene's strain distribution. However, removing the top hBN layer creates mechanical asymmetry and relaxes boundary conditions that stabilize strain distribution [36, 37]. As a result, graphene undergoes local strain redistribution when the top encapsulant is removed, following strain transfer mechanisms similar to those in thin-film structures [38]. Notably, strain distribution does not change significantly after brooming, but the two clusters in figure 3(f) move closer due to reduced and more uniform doping.

Next, we characterized exposed regions using low-temperature quantum transport, comparing its quality with previous measurements before etching and in fully encapsulated regions. The blue curve in figure 4(a) plots the mobility extracted from the Drude conductivity measured at 10 K before etching. It shows mobilities larger than 400,000 cm^{2}V^{-1}s^{-1} over the entire doping range. In pristine graphene heterostructures, the channel is so clean that carriers do not scatter until reaching device edges, resulting in a mobility limited by the device width [23, 24]. The green solid line in figure 4(a) plots the width-limited mobility corresponding to our devices ($w = 8$ μm). For hole doping ($n < 0$), mobilities reach this limit demonstrating excellent electronic quality. For electron doping mobility is slightly less, potentially due to impurities in the hBN substrate. Because of the excellent electronic quality, our devices exhibited clear signatures of ballistic transport, including magnetic focusing [39–41] and negative bend resistance [7].

The AFM and Raman data from D1_window2 are particularly promising, suggesting high-quality graphene can be preserved even after removing top hBN provided AFM brooming [26, 27] is employed. To benchmark electronic quality, we performed low-temperature quantum magneto-transport measurements, comparing device characteristics before and after opening the windows. The pink data in figure 4(a) plots the mobility of our device measured at 10 K in the same region, using the same contact pairs, before the window

was opened (inset of figure 1(a)). While the mobility decreases for all the doping, it still remains relatively high $> 200{,}000$ cm^2 V^{-1}s^{-1}, competitive with the state-of-the-art reports of graphene on hBN without encapsulation [6, 42]. Even with pristine etching that avoids graphene fluorination, some degradation may be expected because the graphene is now exposed to atmospheric conditions and may be sensitive to absorbates.

To further assess device quality, we performed magnetic focusing experiments [39–41] (inset of figure 4(b)). These measurements serve as an excellent characterization tool, tracking ballistic trajectories of semi-classical quasi-particles exhibiting Lorenz-like motion. The measurement geometry is sketched in the inset of figure 4(b). In magnetic focusing experiments, ballistic carriers injected at side contacts are curved by finite magnetic fields and collected at adjacent electrodes. For specific values of magnetic field, when the semi-classical cyclotron radius is commensurate with contact spacing, resistance peaks appear. We choose a geometry that tracks ballistic properties through the etched region. An example of the resonances can be seen clearly in the inset of figure 4(b) showing an oscillatory structure appearing for one sign of the magnetic field. Figure 4(b) plots the magnetic focusing resistance R_{TMF} as a function of magnetic field (B) and carrier density (n). Notably, strong magnetic focusing resonances can be observed for electron and hole doping. For hole doping, higher-order resonances corresponding to multiple reflections from device edges are visible up to $p = 5$. The observation of magnetic focusing demonstrates the excellent quality of our devices even after removal of the top hBN. To our knowledge, this is the first demonstration of ballistic transport over micron-length scales in single-sided graphene encapsulation. To further characterize the ballistic properties, we performed bend resistance measurements. The geometries are sketched in the inset of figure 4(c). For V_1 we observe a strong negative bend resistance appears with doping indicating carriers propagate ballistically across the device over 8 μm. In V_2 the negative response was strongly suppressed, likely due to trajectories passing through the etched region where the mobility is lower (figure 4(a)). Nonetheless, ballistic carriers remain detectable (figure 4(c) inset). The strong negative bend resistance in V_1 confirms that unetched regions retain high electronic quality after SF_6 treatment. Similar observations were made near D1_window1. Although mobility degradation was more severe due to surface contamination, high-order magnetic focusing features remained visible, corresponding to trajectories avoiding the window region (see supplementary section 4). This further demonstrates that high electronic quality is preserved in unetched regions.

Figure 4(a) shows that carrier mobility does not degrade significantly at 10 K and remains high across the doping range. For device applications, assessing quality at room temperature is also crucial. Figure 4(d) plots mobility measured in the etched region (D1_window2) and pristine fully encapsulated regions at 300 K. At these temperatures, mobility appears largely unaffected by opening a window in the hBN, remaining nearly identical for hole doping. We attribute this behavior to dominant phonon contributions, which limit graphene's intrinsic mobility. In other words, at room temperature, etched regions approach the intrinsic mobility limits of graphene encapsulated with hBN [11] with competitive values $> 50{,}000$ cm^{2}V^{-1}s^{-1}.

1. Discussion

Our measurements show that clean *in-situ* patterning of top hBN in van der Waals heterostructures can be made without significantly degrading the electronic quality of underlying 2D layers. AFM measurements confirm that pristine surfaces can be opened if AFM brooming is performed. Our experiments showed that this step is essential in obtaining clean surfaces after etching with < 1 nm surface roughness (figures 2(a) and (b)). However, some variability in achievable surface roughness on the sub nanometer scale remains to be understood. The cleanest windows were observed in D2_window3 (figure 2(c)) and D3_window4 (supplementary section 2), showing regions of atomically flat surfaces (< 200 pm). This enhanced quality compared to D1_window2 may be due to several factors. First, molecular adsorbates may contribute to the surface roughness [43]. Second, the AFM brooming conditions may require further optimization, depending on the number of pre-etching steps involving PMMA deposition. In D1, polymer masks were deposited and washed twice for opening D1_window1 and then D1_window2. In contrast, D2_window3 and D3_window4 underwent one etching procedure, uniquely defined on different devices. Furthermore, the PMMA mask was not removed after etching in D3_window4. In summary, D2/D3 generally faced less exposure to PMMA contamination than D1. This step may be important for achieving the atomically pristine surfaces, as washing in solvents can lead to nanoscale contaminants adsorbing onto the window region. Nonetheless, residual PMMA can still be removed through high-temperature annealing. This was evident in D2_window3 which showed a vast improvement in surface roughness post-annealing (see supplementary section 7). Further work is needed to optimize processing steps for reproducing pristine atomic surfaces.

In some applications, selective etching may be needed before depositing contacts, such as when 2D contacts to exposed graphene are required. In this case, Raman spectroscopy can characterize graphene quality due to its sensitivity to fluorination, serving as an initial screening of the active 2D layer before contact deposition. Strong fluorination is typically detected through the appearance of D' peaks [44, 45].

However, previous studies required long exposure times to resolve Raman signatures. Our etching recipes use significantly shorter times, lasting minutes rather than hours. Thus, it is unsurprising that excess fluorination is not observed. However, low-temperature quantum transport measurements show slight quality degradation. When plotting resistivity as a function of carrier doping (see supplementary section 5), we notice peak splitting at the Dirac point, suggesting doping inhomogeneities in the sample. This may result from slight fluorination undetectable by Raman signals or surface contaminants. Notably, brooming the device surface after etching seemingly restored pristine quality (figure 3(d)/(f)), indicating degradation likely originates from surface contamination. While there may be some minute/undetectable damage to graphene due to electron irradiation, we believe it is much less compared to what is normally induced via dry etching or chemical processes, and hence not relevant in the context of our work.

Finally, we note that over-etching can degrade graphene´s electronic quality. This was evident in D2_window3, where we intentionally over-etched for 2 min. Raman and quantum transport measurements on this sample showed strong doping inhomogeneities post-etching (see supplementary section 6). This experiment highlights the need for careful calibration of etching procedures and demonstrates that room-temperature Raman spectroscopy effectively probes surface quality in exposed graphene, even without the presence of D' bands. However, the surface can be further treated through high-temperature annealing (600° C in vacuum). This is evident in Raman spectroscopy measurements performed on D3 before and after annealing (see supplementary section 6), showing that doping and strain profiles change post-annealing. Additionally, annealing at moderate temperatures (250° C in an argon-hydrogen mixture with 10% H_2) may help reverse fluorination effects [44].

2. Conclusion

Our experiments outline a new technique for engineering the top encapsulating hBN in van der Waals heterostructures. We demonstrate the technique can be used to open windows into graphene encapsulated with hexagonal-boron nitride, while preserving the electronic quality of the 2D surface. Aside from hBN, preliminary experiments on selectively etching transition-metal dichalcogenides (see supplementary section 8), show that high quality of underlying graphene can also be preserved, highlighting the broader applicability to graphene encapsulated with 2D semiconductors [46]. The technique has strong prospects in scanning probe microscopy, enabling the possibility to access fully encapsulated quantum transport devices to bridge the gap in understanding between global and local measurements. With further optimization, the procedure offers a more controllable method for obtaining pristine surfaces compared to the stack-and-flip method currently employed [20]. Cryogenic techniques may further enhance controllability and resolution in advanced nano-patterned structures [47]. It may also be used in scattering near-field optical microscopy (SNOM) experiments, enhancing the light-matter coupling between the tip and the underlying substrate [48]. From an application perspective, the capability to pattern the top hBN offers exciting opportunities. Aside from chemical sensing, it offers unique directions in 2D meta-materials [49] including engineering of polaritonic launches, excitonic landscapes, advanced [50] and artificial superlattice structures [51, 52].

3. Methods

3.1. Device fabrication

The samples are fabricated using typical methods in heterostructure assembly. Typically, a thin hBN flake (∼10–15 nm) is picked using hot-pick up technique [22, 53] using a polypropylene carbonate (PC) film on a polydimethylsiloxane (PDMS) stamp at 90° C. This hBN flake is then later used to pick up the graphene monolayers, mechanically exfoliated on Si^{++}/SiO_2 (285 nm) from highly oriented pyrolytic graphite, and pre-characterized using optical microscopy, and Raman spectroscopy [28]. In D3, twisted graphene was assembled between hBN layers and an additional graphite layer was picked up after the bottom hBN. Finally, the stack is used to pick up a last layer of hBN and later dropped on a pre-patterned marker chip of Si^{++}/SiO_2 (285 nm) at 180° C, squeezing out the bubbles, and impurities as previously reported. The stack is then shaped into a Hall bar geometry using SF_6 plasma, O_2 plasma to etch top hBN, and graphene respectively, and further metalized using 3/15/30 nm of Cr/Pd/Au. The thickness of hBN flakes is identified by their color shading through optical contrast in a microscope, and consequently via AFM when assembled in the heterostructure. The heights can be distinguished from steps in the height profiles induced by exposed graphene edges.

3.2. SF_6 etching rates

The etching was performed in an OXFORD or SAMCO RIE (see supplementary information 1 for detailed recipe). For D1_window1, D1_window2, and D2_Window3, etching were done in OXFORD RIE with hBN

etch rate of ∼ 7 nm/min. For D3_window4, etching was done in SAMCO RIE with hBN etch rate of ∼ 5 nm/min. Before etching, the RIE chamber was pre-conditioned for 15 min with the same SF_6 recipe.

3.3. Raman spectroscopy

Raman spectroscopy measurements were performed at room temperature using a 532 nm laser with optical power of 0.5 mW, focused on a 500 nm spot.

3.4. Quantum transport

Low-temperature quantum transport measurements were performed on an Advanced Research Systems 4 K Cryostat. Measurements were performed using standard lock-in techniques (SR 860) in constant current mode sourcing a small AC current (<100 nA) while measuring the four-probe voltage. For magnetic field measurements, a 1 T electromagnet was used (GMW associates).

Data availability statement

All data supporting the findings of this study are publicly available under the Creative Commons Attribution 4.0 International License (CC-BY 4.0) via Zenodo at: https://doi.org/10.5281/zenodo.15869927 (reference [54]). Additional data including those from the Supplementary Information are available from the corresponding authors upon request.

Acknowledgments

We would like to thank Carmen Rubio-Verdú (ICFO), Tymofiy Khodkov (ICFO), Lene Gammelgaard (DTU), Juan Sierra, Patricia Aguilar, Sergio Valenzuela (ICN2) and Qian Yang (University of Manchester) for important insights and useful discussions. We further thank Matteo Ceccanti for making the illustration presented in figure 1. H.A. acknowledges funding from the European Union's Horizon 2020 research and innovation programme under Marie Skłodowska-Curie grant Agreement No. 665884. A.R.-P. acknowledges funding from ANR JCJC NEAR-2D and Welcome Package Idex (UniCA) as well as AAP Tremplin Complex 2023 '2DNEUROTWIST' (ANR-15-IDEX-01). R.K.K. acknowledges funding by MCIN/AEI/10.13039/501100011033 and by the 'European Union NextGenerationEU/PRTR' PCI2021-122020-2A within the FLAG-ERA grant [PhotoTBG], by ICFO, RWTH Aachen and ETHZ/Department of Physics.
R. K. K. also acknowledges support from the Ramon y Cajal Grant RYC2022-036118-I funded by MICIU/AEI/10.13039/501100011033 and by 'ESF+'. F.H.L.K. acknowledges support from the Gordon and Betty Moore Foundation through Grant GBMF12212, and the Government of Spain (QTWIST RD0768/2022, PID2022-141081NB-I00; Severo Ochoa CEX2019-000910-S, and CEX2024- 001490-S [MCIN/ AEI/10.13039/501100011033). This work was also supported by the European Union NextGenerationEU/PRTR (PRTR-C17.I1) and EXQIRAL 101131579, Fundació Cellex, Fundació Mir-Puig, Generalitat de Catalunya (CERCA, Department of Digital Policies and Territory, AGAUR, 2021 SGR 014431656), and BBVA Foundation 2022 Fundamentals Program (An Electronic Quantum Simulator). Views and opinions expressed are those of the author(s) only and do not necessarily reflect those of the European Union Research Executive Agency. Neither the European Union nor the granting authority can be held responsible for them. This material is based upon work supported by the Air Force Office of Scientific Research under Award Number FA8655-23-1-7047. Any opinions, findings, conclusions, or recommendations expressed in this material are those of the author(s) and do not necessarily reflect the views of the United States Air Force.

ORCID iDs

Hitesh Agarwal 0000-0002-9418-7966
Antoine Reserbat-Plantey 0000-0002-9106-8750
David Barcons Ruiz 0000-0002-6271-2244
Karuppasamy Pandian Soundarapandian 0000-0002-9664-9095
Vahagn Mkhitaryan 0000-0002-3138-8488
Johann Osmond 0000-0001-6522-4695
Kenji Watanabe 0000-0003-3701-8119
Petr Stepanov 0000-0002-1121-3146
Frank H L Koppens 0000-0001-9764-6120
Roshan Krishna Kumar 0000-0003-0857-4466

References

[1] Kubota Y, Watanabe K, Tsuda O and Taniguchi T 2007 Deep ultraviolet light-emitting hexagonal boron nitride synthesized at atmospheric pressure *Science* **317** 932–4
[2] Zhang K, Feng Y, Wang F, Yang Z and Wang J 2017 Two dimensional hexagonal boron nitride (2D-hBN): synthesis, properties and applications *J. Mater. Chem. C* **5** 11992–2022
[3] Molaei M J, Younas M and Rezakazemi M 2021 A comprehensive review on recent advances in two-dimensional (2D) hexagonal boron nitride *ACS Appl. Electron. Mater.* **3** 5165–87
[4] Moon S, Kim J, Park J, Im S, Kim J, Hwang I and Kim J K 2023 Hexagonal boron nitride for next-generation photonics and electronics *Adv. Mater.* **35** 2204161
[5] Young A F, Dean C R, Meric I, Sorgenfrei S, Ren H, Watanabe K, Taniguchi T, Hone J, Shepard K L and Kim P 2012 Electronic compressibility of layer-polarized bilayer graphene *Phys. Rev. B* **85** 235458
[6] Dean C R *et al* 2010 Boron nitride substrates for high-quality graphene electronics *Nat. Nanotechnol.* **5** 722–6
[7] Mayorov A S *et al* 2011 Micrometer-scale ballistic transport in encapsulated graphene at room temperature *Nano Lett.* **11** 2396–9
[8] Liu Y, Weiss N O, Duan X, Cheng H-C, Huang Y and Duan X 2016 Van der Waals heterostructures and devices *Nat. Rev. Mater.* **1** 16042
[9] Andrei E Y, Efetov D K, Jarillo-Herrero P, MacDonald A H, Mak K F, Senthil T, Tutuc E, Yazdani A and Young A F 2021 The marvels of moiré materials *Nat. Rev. Mater.* **6** 201–6
[10] Neumann C *et al* 2015 Raman spectroscopy as probe of nanometre-scale strain variations in graphene *Nat. Commun.* **6** 8429
[11] Wang L *et al* 2013 One-dimensional electrical contact to a two-dimensional material. science (1979) *Science* **342** 614–7
[12] Koepfli S M *et al* 2024 Controlling photothermoelectric directional photocurrents in graphene with over 400 GHz bandwidth *Nat. Commun.* **15** 7351
[13] Liu Y, Dong X and Chen P 2012 Biological and chemical sensors based on graphene materials *Chem. Soc. Rev.* **41** 2283–307
[14] Guarochico-Moreira V H *et al* 2022 Tunable spin injection in high-quality graphene with one-dimensional contacts *Nano Lett.* **22** 935–41
[15] Wong D, Nuckolls K P, Oh M, Lian B, Xie Y, Jeon S, Watanabe K, Taniguchi T, Bernevig B A and Yazdani A 2020 Cascade of electronic transitions in magic-angle twisted bilayer graphene *Nature* **582** 198–202
[16] Choi Y *et al* 2019 Electronic correlations in twisted bilayer graphene near the magic angle *Nat. Phys.* **15** 1174–80
[17] Xue J, Sanchez-Yamagishi J, Bulmash D, Jacquod P, Deshpande A, Watanabe K, Taniguchi T, Jarillo-Herrero P and LeRoy B J 2011 Scanning tunnelling microscopy and spectroscopy of ultra-flat graphene on hexagonal boron nitride *Nat. Mater.* **10** 282–5
[18] Rubio-Verdú C *et al* 2022 Moiré nematic phase in twisted double bilayer graphene *Nat. Phys.* **18** 196–202
[19] Utama M I B *et al* 2021 Visualization of the flat electronic band in twisted bilayer graphene near the magic angle twist *Nat. Phys.* **17** 184–8
[20] Lisi S *et al* 2021 Observation of flat bands in twisted bilayer graphene *Nat. Phys.* **17** 189–93
[21] Grenadier S, Li J, Lin J and Jiang H 2013 Dry etching techniques for active devices based on hexagonal boron nitride epilayers *J. Vac. Sci. Technol. A.* **31** 061517
[22] Pizzocchero F, Gammelgaard L, Jessen B S, Caridad J M, Wang L, Hone J, Bøggild P and Booth T J 2016 The hot pick-up technique for batch assembly of van der Waals heterostructures *Nat. Commun.* **7** 11894
[23] Kumaravadivel P *et al* 2019 Strong magnetophonon oscillations in extra-large graphene *Nat. Commun.* **10** 3334
[24] Wang W *et al* 2023 Clean assembly of van der Waals heterostructures using silicon nitride membranes *Nat. Electron.* **6** 981–90
[25] Lindvall N, Kalabukhov A and Yurgens A 2012 Cleaning graphene using atomic force microscope *J. Appl. Phys.* **111** 064904
[26] Rosenberger M R, Chuang H-J, McCreary K M, Hanbicki A T, Sivaram S V and Jonker B T 2018 Nano-"squeegee" for the creation of clean 2D material interfaces *ACS Appl. Mater. Interfaces* **10** 10379–87
[27] Goossens A M *et al* 2012 Mechanical cleaning of graphene *Appl. Phys. Lett.* **100** 073110
[28] Ferrari A C *et al* 2006 Raman spectrum of graphene and graphene layers *Phys. Rev. Lett.* **97** 187401
[29] Gorbachev R V *et al* 2011 Hunting for monolayer boron nitride: optical and Raman signatures *Small* **7** 465–8
[30] Basko D M, Piscanec S and Ferrari A C 2009 Electron-electron interactions and doping dependence of the two-phonon Raman intensity in graphene *Phys. Rev. B* **80** 165413
[31] Eckmann A, Felten A, Mishchenko A, Britnell L, Krupke R, Novoselov K S and Casiraghi C 2012 Probing the nature of defects in graphene by raman spectroscopy *Nano Lett.* **12** 3925–30
[32] Blake P, Hill E W, Castro Neto A H, Novoselov K S, Jiang D, Yang R, Booth T J and Geim A K 2007 Making graphene visible *Appl. Phys. Lett.* **91** 063124
[33] Yoon D, Moon H, Son Y-W, Choi J S, Park B H, Cha Y H, Kim Y D and Cheong H 2009 Interference effect on Raman spectrum of graphene on SiO_2/Si *Phys. Rev. B* **80** 125422
[34] Reserbat-Plantey A, Klyatskaya S, Reita V, Marty L, Arcizet O, Ruben M, Bendiab N and Bouchiat V 2013 Time- and space-modulated Raman signals in graphene-based optical cavities *J. Opt.* **15** 114010
[35] Lee J E, Ahn G, Shim J, Lee Y S and Ryu S 2012 Optical separation of mechanical strain from charge doping in graphene *Nat. Commun.* **3** 1024
[36] Vincent T, Panchal V, Booth T, Power S R, Jauho A-P, Antonov V and Kazakova O 2019 Probing the nanoscale origin of strain and doping in graphene-hBN heterostructures *2D Mater.* **6** 015022
[37] Peña T, Chowdhury S A, Azizimanesh A, Sewaket A, Askari H and Wu S M 2021 Strain engineering 2D MoS_2 with thin film stress capping layers *2D Mater.* **8** 045001
[38] Schadler L S and Noyan I C 1991 Experimental determination of the strain transfer across a flexible intermediate layer in thin film structures as a function of flexible layer thickness *MRS Online Proc. Library* **239** 151–6
[39] Berdyugin A I *et al* 2024 Minibands in twisted bilayer graphene probed by magnetic focusing *Sci. Adv.* **6** eaay7838
[40] Lee M *et al* 2016 Ballistic miniband conduction in a graphene superlattice *Science* **353** 1526–9
[41] Taychatanapat T, Watanabe K, Taniguchi T and Jarillo-Herrero P 2013 Electrically tunable transverse magnetic focusing in graphene *Nat. Phys.* **9** 225–9
[42] Amet F, Bestwick A J, Williams J R, Balicas L, Watanabe K, Taniguchi T and Goldhaber-Gordon D 2015 Composite fermions and broken symmetries in graphene *Nat. Commun.* **6** 5838
[43] Temiryazev A, Frolov A and Temiryazeva M 2019 Atomic-force microscopy study of self-assembled atmospheric contamination on graphene and graphite surfaces *Carbon Capture Sci. Technol.* **143** 30–37
[44] Nair R R *et al* 2010 Fluorographene: a two-dimensional counterpart of Teflon *Small* **6** 2877–84

[45] Withers F, Russo S, Dubois M and Craciun M F 2011 Tuning the electronic transport properties of graphene through functionalisation with fluorine *Nanoscale Res. Lett.* **6** 526
[46] Soundarapandian K P, De Fazio D, Bernal-Texca F, Hoffmann R, Ceccanti M, De Bonis S L, Tongay S and Koppens F H L 2023 Hysteresis-free high mobility graphene encapsulated in tungsten disulfide *Appl. Phys. Lett.* **123** 063103
[47] Xu J *et al* 2024 Deep-reactive ion etching of silicon nanowire arrays at cryogenic temperatures *Appl. Phys. Rev.* **11** 021411
[48] Hesp N C H *et al* 2021 Observation of interband collective excitations in twisted bilayer graphene *Nat. Phys.* **17** 1162–8
[49] Danielsen D R, Lyksborg-Andersen A, Nielsen K E S, Jessen B S, Booth T J, Doan M-H, Zhou Y, Bøggild P and Gammelgaard L 2021 Super-resolution nanolithography of two-dimensional materials by anisotropic etching *ACS Appl. Mater. Interfaces* **13** 41886–94
[50] Kapfer M *et al* 2023 Programming twist angle and strain profiles in 2D materials *Science* **381** 677–81
[51] Forsythe C, Zhou X, Watanabe K, Taniguchi T, Pasupathy A, Moon P, Koshino M, Kim P and Dean C R 2018 Band structure engineering of 2D materials using patterned dielectric superlattices *Nat. Nanotechnol.* **13** 566–71
[52] Barcons Ruiz D *et al* 2022 Engineering high quality graphene superlattices via ion milled ultra-thin etching masks *Nat. Commun.* **13** 6926
[53] Purdie D G, Pugno N M, Taniguchi T, Watanabe K, Ferrari A C and Lombardo A 2018 Cleaning interfaces in layered materials heterostructures *Nat. Commun.* **9** 5387
[54] Agarwal H *et al* 2025 Data for main text figures - In situ engineering hexagonal boron nitride in van der Waals heterostructures with selective SF6 etching *Zenodo* (https://doi.org/10.5281/zenodo.15869927)